Nano Research

Open Access

Research Article

Super-self-assembly extraction from natural herbs

Jiawei Xiang[1,2,§], Yuan Meng[1,2,§], Mingyuan Zhao[1,2], Zhongxian Li[1], Qiang Zhang[3], Ning Wang[4], Zhuo Ao[1] ✉, and Dong Han[1,2] ✉

[1] *CAS Center for Excellence in Nanoscience, National Center for Nanoscience and Technology, Beijing 100190, China*
[2] *University of Chinese Academy of Sciences, Beijing 100049, China*
[3] *Hebei Key Lab of Nano-biotechnology, Hebei Key Lab of Applied Chemistry, Yanshan University, Qinhuangdao 066004, China*
[4] *Guang'anmen Hospital of the China Academy of Chinese Medical Sciences, Beijing 100053, China*
[§] *Jiawei Xiang and Yuan Meng contributed equally to this work.*

Cite this article: *Nano Research*, **2025**, *18*, 94907094. https://doi.org/10.26599/NR.2025.94907094

ABSTRACT: Life systems are complex systems, and the self-assembly behaviour represents the transition from disorder to order and serves as a concrete indicator and starting point for understanding complex systems. Super-self-assembly behaviour was observed in the decoctions of various natural herbs, and this behaviour was characterized by multistep and multilevel assembly processes. The super-self-assemblies were multilevel particles resulting from inorganic–organic assembly, specifically observed as composite spheres, cubes, and tetragonal bipyramids. The preparation process was environmentally friendly and safe, and the resulting super-self-assemblies were regular in shape and rich in variety; this process has numerous possibilities for development and application in medicine and materials research.

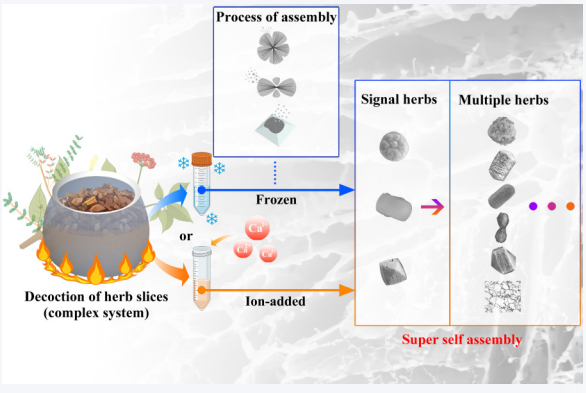

KEYWORDS: self-assembly, natural herbs, multi-morphological particles, complex system

1 Introduction

Complexity science represents a new phase in the development of contemporary systems science. Life systems are complex structures constructed from numerous organic and inorganic molecules, yet they can respond to external stimuli in an orderly manner [1–4]. Living organisms can guide the assembly of organic–inorganic components through organic matter and encapsulate organic substances within assembled structures [1, 5].

The morphogenesis of life from self-assembled structures has evolved over time and space. Compared with homogeneous materials, self-assembled materials can provide rich construction space and multifunctional integration. Therefore, since its discovery, self-assembly has become popular in scientific research and enables the assembly of complex structures through monomer design [6]. Various self-assembly systems have been developed. Biological systems can spontaneously form orderly structures from proteins, polysaccharides, and salts in certain liquid environments. Diverse assembly materials have been constructed in chiral systems [7, 8], using environmental stimuli, such as pH and salt concentration [9], and the liquid–liquid phase separation behaviour of biomimetic polymers [9]. However, artificially manipulating multiple assembly units to form composite hierarchical structures remains challenging.

Herbal decoctions are complex component systems, often do not exist as single compounds, and are assembled into various structures. These naturally occurring assembled structures include assembled nanostructures [10], carbon quantum dots [11], herbal decoctosomes [12], and protein-catechol composite vesicles [13]. These natural assemblies can be used to obtain and improve more materials [12, 14].

In our research, we discovered that aqueous decoctions of various natural herbs could produce multi-morphological particles through simple freeze–thaw processes or through the addition of appropriate ions. Unlike previously reported straight assemblies of purely monomeric molecules [15, 16], the above-mentioned assembly is based on artificially designed molecular assembly [17]. In this study, we found that the particles were formed through a multistep and hierarchical assembly process and could further

Received: August 30, 2024; **Revised:** October 22, 2024
Accepted: October 23, 2024

✉Address correspondence to Zhuo Ao, aoz@nanoctr.cn; Dong Han, dhan@nanoctr.cn

combine during the assembly process to form well-ordered composite particles with the characteristics of the original particles. This indicated that such assemblies are versatile. However, currently, these types of hierarchical assemblies lack a clear name. Compared to similar terms such as co-assembly [18], biomineralization [5], and superstructures [19, 20], the main components of the freeze–thaw products we obtained were always defined, and their structures were more diverse (Figs. S9 and S10 in the Electronic Supplementary Material (ESM)). Therefore, we referred to these structures as "super-self-assembly" (Fig. 1), as this term was more universal. The preparation methods for super-self-assemblies are simple and environmentally friendly, providing a significant complement to current advancements in medicine, physics, and materials sciences.

2 Experimental

2.1 Materials and preparation

2.1.1 Materials

Calcium sulfate dihydrate and anhydrous calcium chloride were purchased from Xilong Chemical Co., Ltd. Polyethylene glycol 400 (PEG 400) was acquired from Aladdin Reagent Co., Ltd., Shanghai, China. Gelatine from porcine skin was obtained from Sigma-Aldrich Trading Co., Ltd., Shanghai, China. Bovine serum albumin V was purchased from Beijing Chengxin Kangrun Medical Equipment Co., Ltd., Beijing, China. Neutral red reagent was purchased from Macklin Biochemical Co., Ltd., Shanghai, China. Doxorubicin hydrochloride was purchased from Beijing Hvsf United Chemical Materials Co., Ltd., Beijing, China. Cell counting kit-8 (CCK-8) and dialysis bags were purchased from Beijing Solarbio Science & Technology Co., Ltd., Beijing, China. Reactive oxygen species assay kit was purchased from BestBio Biotechnology Co., Ltd., Shanghai, China. Herbs slices were all sourced from Beijing Tongrentang, Beijing, China.

2.1.2 Cell culture and related experiments

RAW264.7 macrophage cell lines were obtained from the Cell Bank of the Chinese Academy of Sciences, Shanghai, China. The RAW264.7 macrophages were cultured in Dulbecco's modified Eagle's medium (DMEM) supplemented with foetal bovine serum (FBS, 10% v/v; Thermo Fisher Scientific) and antibiotic-antifungal solution (1% v/v; Thermo Fisher Scientific) at 37 °C in a 5% CO_2 atmosphere. To avoid contamination, the prepared *Achyranthis Bidentatae Radix* (NX) particles were sterilized by being placed in a 100 °C water bath for 30 min before administration.

2.2 Experimental methods

2.2.1 Sample preparation

Fifty grams of each herbal slice was weighed and placed in a decoction pot. Double-distilled water was added to cover the slices, and the slices were soaked for 1 h. The herbs were subsequently boiled for 1 h. After boiling, the decoction mixture was collected and centrifuged at 10,000*g* to remove the herbal residues. Finally, the supernatant was collected and stored at −20 °C overnight (12–24 h). The supernatant was subsequently thawed and centrifuged again at 10,000*g*. Afterwards, the precipitate was observed. The precipitate was resuspended in double-distilled water and washed by centrifugation. The precipitate obtained consisted of super-self-assembled particles (Fig. 2).

2.2.2 Physicochemical characterization of super-self assembled particles

A total of 20 μL of each particle suspension was removed and added dropwise onto a silicon wafer. They were allowed to air dry naturally. After drying, the samples were coated with gold for 30 s using an ion sputter coater. The samples were subsequently observed using scanning electron microscopy (SEM, Hitachi S4800+EDS).

A total of 10 μL of each particle suspension was added dropwise onto a carbon support film. The samples were incubated for

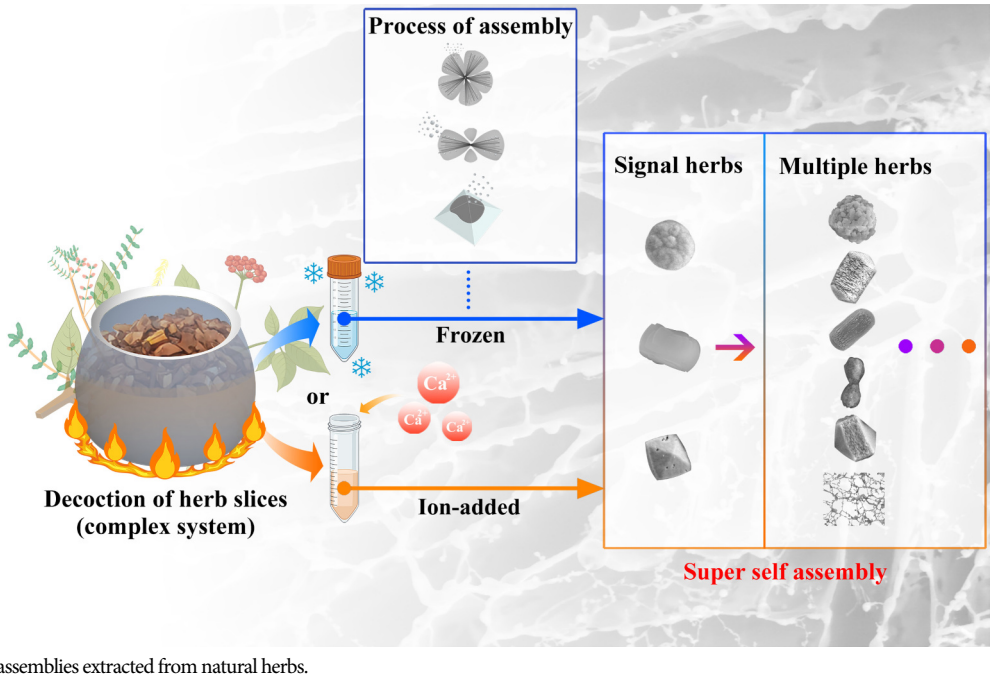

Figure 1 Super-self-assemblies extracted from natural herbs.

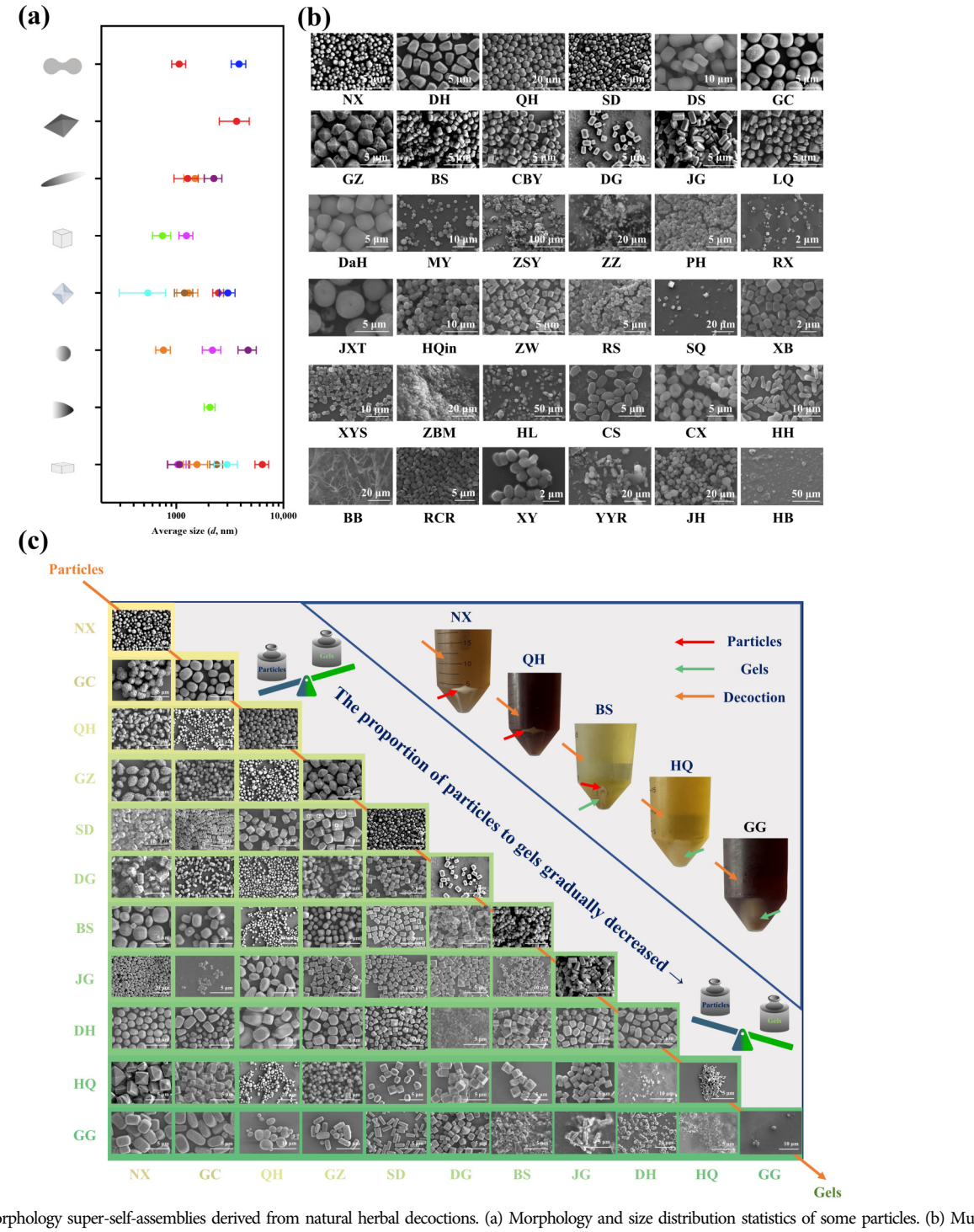

Figure 2 Multi-morphology super-self-assemblies derived from natural herbal decoctions. (a) Morphology and size distribution statistics of some particles. (b) Multi-morphology super-self-assemblies, including particles and fibrous gel network structures. (c) Multi-morphology super-self-assemblies obtained from decoctions of paired herbal slices after the freeze–thaw process.

10 min, and qualitative filter papers were used to absorb the excess liquid. The films were dried at 37 °C. The particles were observed using both transmission electron microscopy (TEM, T20, Tecnai G2 20 S-TWIN) and field emission-TEM (FE-TEM, Tecnai G2 F20 U-TWIN).

The gel substances were observed using environmental SEM (ESEM, Quanta 200 FEG) after freezing.

Specifically, for the NX particles, *Glycyrrhizae Radix Et Rhizoma* (GC) particles, and *Notopterygii Rhizoma Et Radix* (QH) particles, energy dispersive X-ray spectroscopy (EDS) was performed to obtain their mapping images of C, O, N, and Ca. The sizes of the NX particles, GC particles and QH particles were statistically determined from the SEM images using Fiji software (Fig. 3(b)). The three types of particles were suspended in pure water and placed in a zeta potential measurement cell; their zeta potentials were measured using a Malvern Zetasizer (Fig. 3(c)).

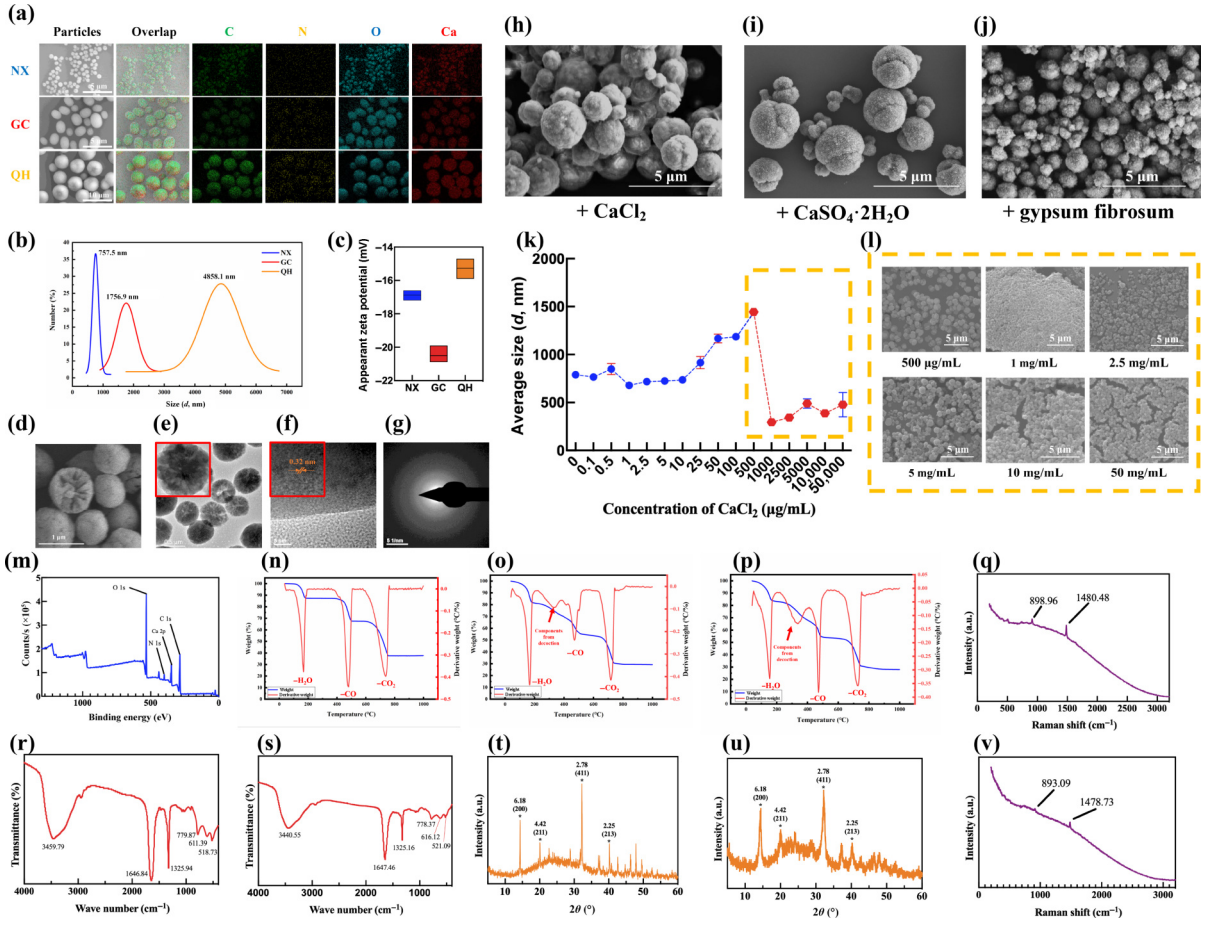

Figure 3 Exploration of the physical and chemical characterization and formation mechanism of super-self-assembled particles. (a) Morphology of the three types of spherical particles (NX, GC, and QH) under SEM, along with elemental analysis mapping by EDS. (b) Particle size distribution graphs of the NX, GC, and QH particles. The particle sizes of NX and GC were determined by dynamic light scattering (DLS), whereas those of QH were obtained by using fitting the results from the electron microscopy analysis. (c) Distribution of the zeta potentials of the NX, GC, and QH particles. (d) SEM image of the NX particles. (e) TEM images of the NX particles. The inset shows an enlarged image of the NX particles. (f) HRTEM images of the NX particles. The inset shows the internal lattice arrangements of the NX particles. (g) Electron diffraction pattern of the NX particles using TEM. (h) SEM images of particles obtained by adding $CaCl_2$ solution to the supernatant of the NX decoction. (i) SEM images of the particles obtained by adding a $CaSO_4{\cdot}2H_2O$ solution to the supernatant of the NX decoction. (j) SEM images of the particles obtained by adding the filtrate of the gypsum fibrosum decoction to the supernatant of the NX decoction. (k) Relationship between the average particle size of the NX particles and the concentration of $CaCl_2$ added to the supernatant of the NX decoction. Vertical axis: average particle size. Horizontal axis: concentration of $CaCl_2$ in the decoction solution after adding $CaCl_2$ solution. The blue curve represents the particles obtained after freezing. The red curve represents the particles directly precipitated from the solution. (l) SEM morphology of the NX particles precipitated from the decoction at different concentrations of $CaCl_2$ (500–50,000 μg/mL). (m) XPS spectrum of the NX particles. (n) TG curve (blue curve) and DTG curve (red curve) of pure calcium oxalate hydrate. (o) TG curve (blue curve) and DTG curve (red curve) of the NX particles obtained after the freeze–thaw process. (p) TG curve (blue curve) and DTG curve (red curve) of the NX particles obtained from the addition of calcium. (q) Raman spectrum of the NX particles obtained after the freeze–thaw process. (r) IR spectrum of the NX particles obtained after the freeze–thaw process. (s) IR spectrum of the NX particles obtained from the addition of calcium. (t) XRD spectrum of the NX particles obtained after the freeze–thaw process. (u) XRD spectrum of the NX particles obtained from the addition of calcium. (v) Raman spectrum of the NX particles obtained from the addition of calcium.

The dried NX particles were analysed by X-ray photoelectron spectroscopy (XPS, ESCALAB250Xi) to determine the surface elemental composition (Fig. 3(m)). Additionally, KBr pellets were prepared for infrared (IR) spectroscopy (spotlight 200i). The IR spectra were recorded over the range of 400 to 4000 cm^{-1}, with a resolution of 4 cm^{-1} and the accumulation of over 8 scans (Figs. 3(r) and 3(s), and Fig. S7(d) in the ESM).

The dried samples were subjected to thermogravimetric analysis (TGA, TG 209F3). The analysis was conducted at an initial temperature of 40 °C and a final temperature of 1000 °C under a nitrogen atmosphere with a heating rate of 10 °C/min (Figs. 3(n)–3(p)).

The dried samples were filled into the sample holder and analysed using X-ray diffraction (XRD, D/MAX-TTRIII(CBO)). The scan parameters were as follows: start angle of 4°, stop angle of 80°, and scan speed of 5°/min (Figs. 3(t), 3(u), and 4(d), and Fig. S7(e) in the ESM).

The dried NX particles were sent for Raman spectroscopy (Renishaw) analysis (Figs. 3(q) and 3(v)).

Finally, the collected NX particles were sent for organic elemental analysis (varioELcube) to determine the contents of N, C, H, and S elements.

2.2.3 *Formation process and elemental distribution of super-self-assembled particles*

The supernatants from the QH, *Salviae Miltiorrhizae Radix Et Rhizoma* (DS), and *Cinnamomi Ramulus* (GZ) decoctions were frozen at −20 °C for 30 min. After thawing, the mixture was

centrifuged, the supernatant was discarded, and the precipitate was resuspended. The resuspended precipitate was added dropwise onto a carbon support film, and the images were captured using TEM and FE-TEM. The images obtained were compared and aligned with those from SEM to illustrate the particle formation process. FE-TEM was used to observe the particles in high-angle annular dark field (HAADF) mode, and TEM-EDS mapping was performed on the edges of the particles. For the GZ particles, line scanning was conducted. Finally, the data were analysed to produce the final graphical representation (Fig. 4).

2.2.4 Relationship between the NX particle size and formation with added $CaCl_2$

For the NX decoction prepared by the above method, 9 mL aliquots of the supernatant was mixed with 1 mL of the $CaCl_2$ solutions to obtain solutions with final $CaCl_2$ concentrations of 0, 0.1, 0.5, 1, 2.5, 5, 10, 25, 50, and 100 μg/mL. The solutions were subsequently frozen at −20 °C and then thawed after 12 h of freezing. The particles were collected for particle size analysis using a Malvern Zetasizer (Zetasizer Nano ZS). When the $CaCl_2$ concentrations in the solutions were 500 μg/mL, and 1, 2.5, 5, 10, and 50 mg/mL, the particles directly precipitated. These particles were collected and imaged using SEM. Then, the particle sizes were analysed with Fiji software. Here, the $CaCl_2$ concentration in the decoction is shown on the horizontal axis, and the particle size is shown on the vertical axis (Fig. 3(k)).

2.2.5 Morphological control and drug loading capacity of the NX particles

Fifty grams of the NX slices were decocted, and the supernatant of the decoction was collected. An excess amount of doxorubicin hydrochloride powder was added to the supernatant. It was dissolved under ultrasonication. Afterwards, the sample was centrifuged at 10,000*g* to remove any undissolved drug precipitates. The supernatant of the decoction was collected again. At this point, the supernatant was a saturated solution of the target drug. A total of 40 mL of the supernatant was removed, and 100 μL of a 200 mg/mL $CaCl_2$ solution was added. The mixture was allowed to stand to allow the formation of the particles. 30 min later, the supernatant containing the precipitated particles was centrifuged at 10,000*g* to collect the precipitate, and the red precipitate was resuspended in double-distilled water to obtain NX-Ca-Dox. Finally, drops of the doxorubicin hydrochloride solution, NX-Ca suspension, and NX-Ca-Dox suspension were added to the silicon wafers and dried. Subsequently, SEM analysis was performed on these samples (Fig. S7(c) in the ESM).

A 0.9% saline injection solution was prepared as the release medium. NX-Ca-Dox was centrifuged to remove the solvent, resuspended in the release medium, and transferred into a dialysis bag. An equal amount of release medium was added outside the dialysis bag, with a molecular weight cut-off of 3500 Da. The solution was stirred at a constant rate in a 37 °C water bath. At

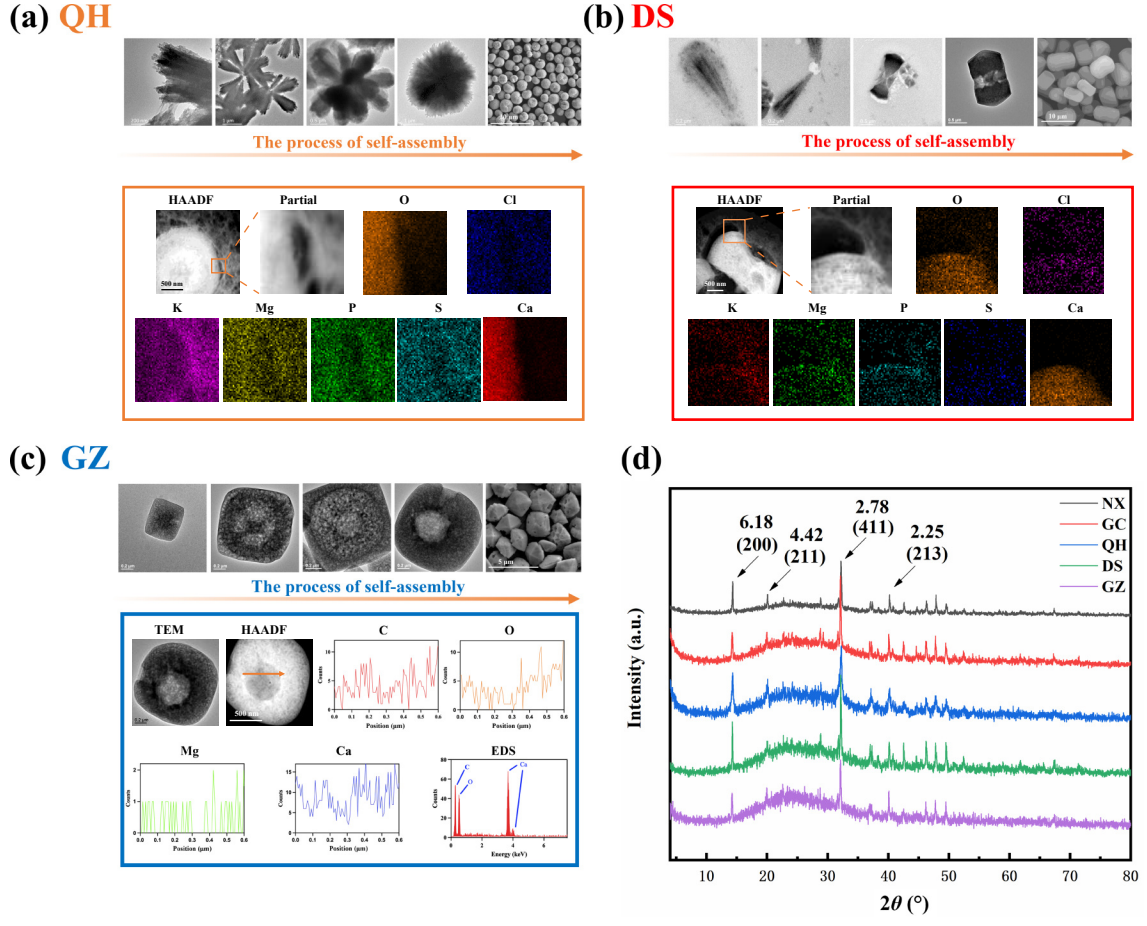

Figure 4 Formation process of super-self-assemblies. (a) Stepwise formation process of the QH super-self-assembled particles and their STEM-EDS mapping analysis. (b) Stepwise formation process of the DS super-self-assembled particles and their STEM-EDS mapping analysis. (c) Stepwise formation process of the GZ super-self-assembled particles and their STEM-EDS line scan analysis. (d) The XRD spectra comparison of NX, GC, QH, DS, and GZ particles.

30 min, and 1, 2, 4, 15, 24, 48, and 72 h, 3 mL of the release medium outside the dialysis bag was removed and replaced immediately with an equal amount of fresh release medium to maintain a constant total volume. The experiment was repeated three times. The content of doxorubicin hydrochloride in the solution was measured using a multifunctional microplate reader with an excitation wavelength of 478 nm and an emission wavelength of 570 nm. The cumulative release rate was calculated and used to create the release curve (Fig. S7(b) in the ESM).

2.2.6 Effects of the NX particles on the RAW264.7 macrophages in vitro

RAW264.7 cells were seeded at 3000 cells/dish. After they were allowed to adhere, *Achyranthis Bidentata* particles were diluted to a concentration of 100 μg/mL in culture medium and incubated with the cells. After 8 h, the samples were fixed overnight with 5% glutaraldehyde solution. The samples were then dehydrated with an ethanol gradient, dried with a CO_2 critical point dryer, sputter-coated with gold, and imaged using SEM (Fig. S8(a) in the ESM).

The RAW264.7 cells were seeded at 3000 cells/well in a 96-well plate. After the cells had adhered, different concentrations of the NX particles were administered and co-incubated for 48 h. The culture medium was then removed, and 200 μL of 0.1% neutral red solution was added. After 3 h of coincubation, the supernatant was removed, and 200 μL of pure water was added to lyse the cells. The solution was left to stand at 4 °C overnight. The supernatant was then transferred to another 96-well plate, and the absorbance at 490 nm was measured using a multifunctional microplate reader (Fig. S8(b) in the ESM).

RAW264.7 cells were seeded at 3000 cells/well in a 96-well plate. The prepared NX particles were suspended in culture medium at concentrations of 100, 50, 25, 10, 5, 1, and 0.5 μg/mL, 100 μL of these solutions was added to each well, and the sample incubated with the cells. After 24 h, the solution was aspirated, and DMEM containing 10% CCK-8 reagent was added. After 2–3 h, the absorbance at 450 nm was measured via a multifunctional microplate reader (Enspire, Fig. S8(c) in the ESM).

RAW264.7 cells were seeded at 3000 cells/well in a 96-well plate. After the cells had adhered, the NX particles were administered and co-incubated for 24 h. 2',7'-Dichlorodihydrofluorescein diacetate (DCFH-DA) was diluted 1:1000 in serum-free medium, and 100μL of DCFH-DA was added to each well. After incubation at 37 °C for 60 min in a cell culture incubator, the cells were washed with serum-free cell culture medium. The fluorescence intensity of each well was measured using a multifunctional microplate reader with an excitation wavelength of 488 nm and an emission wavelength of 525 nm; these data were used to determine the level of reactive oxygen species (ROS) produced by the cells (Fig. S8(d) in the ESM).

3 Results and discussion

Through the freeze–thaw process, natural herbal decoctions could generate various micro-nanostructures. (Fig. 2(b)). The herbal decoctions used as sources in the figure include NX, *Angelicae Pubescentis Radix* (DH), QH, *Rehmanniae Radix* (SD), DS, GC, GZ, *Paeoniae Radix Alba* (BS), *Platycladi Cacumen* (CBY), *Angelicae Sinensis Radix* (DG), *Platycodonis Radix* (JG), *Forsythiae Fructus* (LQ), *Rhei Radix Et Rhizoma* (DaH), *Myrrha* (MY), *Perillae Folium* (ZSY), *Gardeniae Fructus* (ZZ), *Typhae Pollen* (PH), *Olibanum* (RX), *Spatholobi Caulis* (JXT), *Scutellariae Radix* (HQin), *Asteris Radix Et Rhizoma* (ZW), *Ginseng Radix Et Rhizoma* (RS), *Notoginseng Radix Et Rhizoma* (SQ), *Allii Macrostemonis Bulbus* (XB), *Panacis Quinquefolii Radix* (XYS), *Fritillariae Thunbergii Bulbus* (ZBM), *Coptidis Rhizoma* (HL), *Paeoniae Radix Rubra* (CS), *Chuanxiong Rhizoma* (CX), *Carthami Flos* (HH), *Stemonae Radix* (BB), *Cistanches Herba* (RCR), *Sennae Folium* (XY), *Coicis Semen* (YYR), *Chrysanthemi Flos* (JH), *Phellodendri Chinensis Cortex* (HB), *Astragali Radix* (HQ), and *Puerariae Lobatae Radix* (GG). Due to their multistep and multilevel assembly characteristics, these assembled particles differ from regular self-assembled particles and are called super-self-assemblies. The freeze–thaw products of herbal decoctions mostly appeared in the form of substantial particles. The freeze–thaw products derived from some decoctions, such as BB, showed a gel network structure, whereas those from JG and ZZ had a structure with a mixture of particles and a gel network.

Figure 2(a) presents statistical data on the diverse morphologies and broad particle size distributions of the super-self-assembled particles obtained solely through a simple freeze–thaw process. The particle sizes ranged from several hundred nanometres to a few microns, indicating good monodispersity.

To further investigate the formation patterns of these super-self-assembled structures, we selected 11 herbal slices and mixed them in pairs for co-decoction, followed by a freeze–thaw process. As shown in Fig. 2(c), compared with their original individual products, the products of the mixed herbs exhibited combined morphological changes. This phenomenon could be attributed to the alteration of the matrix environment in the decoction, leading to the formation of a combination of multiple assembly mechanisms.

We arranged the samples based on their changes in their structure types resulting from the freeze–thaw process, as shown in Fig. 2. From the top-left corner to the bottom-right corner of the table, the number of observed particles decreased, whereas the content of gel substances increased (Fig. 2 and Fig. S1 in the ESM). In this study, we found that the particles generated from the HQ and GG decoctions were very few in number and almost invisible and primarily formed gel substances. However, other herbal slices that produced more particles showed changes in particle morphology when they were co-decocted with HQ or GG.

Among them, the decoctions of NX, GC, and QH exhibited a strong ability to produce spheres after the freeze–thaw process. In contrast, the decoctions of SD, BS, JG, DH, and DG tended to form cubes after the same treatment. However, differences in their morphologies and particle sizes were observed. When these herbal slices were co-decocted and subjected to a freeze–thaw process, more complex assembly structures formed. Overall, although these particles exhibited diverse morphologies at the mesoscale, it could be observed that the particles formed from this combination predominantly appear as spheres, cubes, tetragonal bipyramids, and slight variations of these shapes.

Interestingly, the freeze–thaw products of NX&GC, NX&QH, NX&DG, NX&HQ, and QH&GC were formed through further assembly based on their original particle morphologies. These results indicated a multistep and multilevel assembly behaviour. Some herbal slices exhibited unique properties. For example, when combined with other herbal slices, the GZ herbal slices produced particles with more pores, such as GZ&GC, GZ&QH, GZ&SD, and GZ&HQ. Even GZ particles alone tended to form more pores. When co-decocted with other herbal slices, the HQ slices were more likely to form tetragonal bipyramids, with the exception of GZ&HQ. The QH decoction demonstrated a strong ability to form spherical particles, and the particles formed with other slices still

maintained some spherical characteristics, with the exception of SD&QH and DH&QH.

However, the decoctions of the DG, BS, JG, DH, HQ, and GG herbal slices tended to produce more gel substances; these substances covered the potential particles and caused difficulty for their observation. And this phenomenon became more obvious when two herbs were co-decocted, possibly due to the introduction of Fe (Table S1 in the ESM) or other inorganic elements during the combination [21]. Consequently, the freeze–thaw products of BS&GG, HQ&GG, and DH&DG were almost entirely gel substances.

During the collection of assembly structures, particles from NX, GC, and QH were relatively uniform spheres. They could be effectively suspended in water (Fig. S2 in the ESM). Based on the SEM-EDS mapping results, the three types of particles were mainly composed of C, O, and Ca (Fig. 3(a)). The particle sizes of the three types of particles, from smallest to largest, were NX particles, GC particles, and QH particles (Fig. 3(b)). The zeta potentials of all three types of particles were negative (Fig. 3(c)).

Due to the high calcium content of the three types of particles, these particles had similar compositions. Further in-depth studies were conducted on the NX particles. The NX decoction only needed to be frozen at −20 °C for 40–70 min to form a significant number of particles (Fig. S3 in the ESM). The high calcium content in the particles resulted in high contrast under TEM, revealing an internal radial texture structure (Fig. 3(e)). Occasionally, the radial texture structure and substantial core could also be observed using SEM (Fig. 3(d)).

Further observation using high-resolution TEM (HRTEM, Fig. 3(f)) revealed scattered crystalline domains within the particles, indicating that the particles potentially possessed an inorganic framework structure. The observed lattice spacing was 0.32 nm. Additional evidence was provided by the TEM electron diffraction pattern, which showed diffraction rings (Fig. 3(g)). The diffraction pattern was ring shaped and broad, indicating that the particles were locally and short-range ordered. Overall, these particles exhibited an amorphous yet ordered state.

XPS analysis of the NX particles revealed that the surface elements were primarily composed of C, Ca, O, and N, and the surface atomic concentrations obtained were as follows: C: 58.028%, Ca: 6.122%, N: 3.784%, O: 31.465%, P: 0.393%, and S: 0.207% (Fig. 3(m)). Figure 3(o) shows the thermogravimetric (TG) and differential thermogravimetric (DTG) curves of the NX particles. The TG curve indicated minimal weight loss before 100 °C, confirming the good thermal stability of the particles. The TG results indicated that the particles predominantly consisted of calcium oxalate hydrate as the basic framework. Compared with the TG-DTG profile of pure calcium oxalate hydrate (Fig. 3(n)), the rapid weight loss at 336 °C indicated that the particles were not purely calcium oxalate hydrate. The organic components from the herbal decoction participated in the formation of the structure, consisting of more than 15% of the particle mass. Figure 3(r) shows the IR spectrum of the NX particles, and Fig. 3(q) shows the Raman spectrum analysis; both spectra indicated a calcium oxalate hydrate framework. Furthermore, XRD analysis (Fig. 3(t)) of the NX particles obtained from the freeze–thaw process revealed noticeable XRD diffraction peaks, indicating a certain degree of crystalline structure closely matching that of the calcium oxalate hydrate. These results further confirmed the calcium oxalate hydrate framework of the NX particles.

Macroscopically, these particles were insoluble in glacial acetic acid and sodium hydroxide solutions but soluble in hydrochloric acid solutions. Further elemental analysis using an analyser revealed the following elemental mass ratios: N: 0.5%, C: 20.99%, H: 3.95%, and S: 0.09%. These ratios differed from those of pure hydrated calcium oxalate, providing additional evidence that the NX particles formed through freeze–thaw processes possess a composite structure. These particles encapsulated organic substances from the decoction and had calcium oxalate as their frameworks.

The formation of these super-self-assemblies was closely related to the presence of calcium. Adding calcium-containing reagents to the supernatant of the NX decoction could directly induce the formation of spherical particles. Reagent examples included the calcium chloride solution (Fig. 3(h)), the calcium sulfate dihydrate solution (Fig. 3(i)), and the filtrate of the gypsum decoction (Fig. 3(j)). Additionally, when the concentration of the added calcium reagent was relatively low, twin spherical particles were more likely to appear. Figure 3(k) shows the particle size–calcium chloride addition relationship, and Fig. 3(l) shows the SEM images of the precipitated particles at each concentration point.

When the concentration of $CaCl_2$ in the decoction was less than 10 μg/mL, calcium addition had a minimal effect on the particle size of the NX particles. When the concentration of $CaCl_2$ in the decoction was between 10 and 100 μg/mL, the particle size of the NX particles after the freeze–thaw process increased with the addition of calcium. When the $CaCl_2$ concentration in the original solution was between 100 and 500 μg/mL, the particles could precipitate directly after the solution was allowed to stand for a short time; this resulted in larger spherical particles. As the concentration of $CaCl_2$ in the decoction further increased, the particles quickly precipitated, but the precipitated particles became significantly smaller and stabilized at a certain particle size.

The particles obtained by adding calcium were analysed using TG and DTG analyses (Fig. 3(p)). The results indicated that their main structure remained calcium oxalate hydrate, and organic molecules from the solution participated in structure formation. Additionally, the IR spectrum results were similar to those of the original NX particles obtained from the freeze–thaw process (Fig. 3(s)). In the XRD pattern, the peak shapes of the particles were not as sharp as those of the original NX particles obtained from the freeze–thaw process; however, the crystalline peaks of the calcium oxalate hydrate were still visible (Fig. 3(u)). In the Raman spectrum, the peaks became less pronounced; this result was similar to the XRD results. Thus, the crystallinity of the particles obtained by adding calcium was lower than that of the particles obtained through the freeze–thaw process.

The morphology of the NX particles could also be altered by adding chemical reagents to the decoction (Fig. S4 in the ESM). This method could be used to prepare super-self-assembled particles with different morphologies. For example, in the NX + Gelatine group, the formation of these super-self-assembled particles was observed to proceed in a multistep and multilevel manner from the centre to the periphery.

When hydrochloric acid solution was added to the NX particles obtained from the freeze–thaw process or calcium addition, they were dissolved. If sodium hydroxide solution was then added, precipitates formed in the solution. However, under SEM, these particles no longer retained their original morphology (Fig. S5 in the ESM). These results further demonstrated the importance of the decoction solution as a matrix environment in the formation of particle morphology.

The prepared NX super-self-assembled particles had good stability (Fig. S6 in the ESM). By adding calcium ions to the NX decoction, we successfully loaded the NX particles with doxorubicin hydrochloride (Fig. S7 in the ESM), and the loading of doxorubicin hydrochloride was determined to be 2.23% ± 0.17% by fluorescence detection. These particles also demonstrated a certain degree of sustained-release capability (Fig. S7(b) in the ESM), indicating their potential as carriers. These results further confirmed that during the formation of super-self-assembled particles, the substances originally present in the decoction could participate in the assembly of the particles.

We cocultured NX super-self-assembled particles with RAW264.7 macrophages and observed that the macrophages actively phagocytosed the particles; this resulted in a wrinkled surface on the macrophages (Fig. S8(a) in the ESM). Moreover, low concentrations of the NX particles promoted the Swallow activity of the macrophages (Fig. S8(b) in the ESM); this result was consistent with those from the CCK-8 assay, where low concentrations of NX particles increased the cell proliferation activity (Fig. S8(c) in the ESM). ROS detection revealed that different concentrations of the NX particles did not increase reactive oxygen species levels in cells, indicating good biocompatibility of the NX particles (Fig. S8(d) in the ESM). Based on these findings, the NX super-self-assembled particles have potential for pharmaceutical applications.

Based on the above results, super-self-assembled particles primarily exhibited spheres, cubes, and tetragonal bipyramids. To observe their formation process in detail and understand their formation mechanism, we selected QH, DS, and GZ particles; these particles presented microscale spheres, cubes, and tetragonal bipyramids, respectively.

During the short-term freeze–thaw process, we collected the particles and captured their images using TEM. By comparing the intermediate states of the particles with the known final structures, we could determine the particle formation process, as shown in Figs. 4(a)–4(c). Since the particle formation was related to the components in the decoction matrix, we performed scanning transmission electron microscopy-EDS (STEM-EDS) on the surrounding areas or internal structures of the particles without thoroughly washing the sample to explore the elemental composition that interfered with their formation.

First, we used the QH particles as an example. Initially, small crystals aggregated, accompanied by the formation of spindle-shaped structures. These spindle-shaped structures further assembled into flower cluster-like structures. The flower cluster-like structures then gradually became smooth, ultimately forming spheres (Fig. 4(a)).

To investigate the elemental composition of the particles and the surrounding substances (the decoction environment), we allowed the particles to adsorb onto the carbon support films without their thorough washing and analysed the edge areas of the particles using STEM-EDS (Fig. 4(a)). We observed that the decoction environment primarily consisted of C, O, Cl, K, Mg, P, and S, and the majority of the Ca was enriched in the particle region. Interestingly, N was undetected, potentially indicating that the main adsorbates around the particles were not proteins.

The formation of the DS particles was similar to that of the QH particles. Initially, spindle-shaped structures appeared. These spindle-shaped structures further assembled but did not exhibit the radial assembly observed in the QH particles. Instead, they assembled symmetrically at both ends and ultimately formed a cubic morphology. During the process, some low-contrast objects were in contact with the assembling spindle-shaped structures. These objects could participate in the assembly process. Under the illumination of the electron beam, the substances enveloping the particles' exterior expanded, reducing the contrast. STEM-EDS scanning of the edge regions also revealed that the decoction environment primarily consisted of C, O, Cl, K, Mg, P, and S, and Ca was concentrated in the particle region.

The formation of the GZ particles differed slightly from the aforementioned particles. When we first observed the particles, they already exhibited an octahedral morphology. Striations extending from the centre to the periphery of the particles were visible, indicating a specific layered structure. Interestingly, a low-contrast region was observed in the centre of the octahedral particles. Based on the STEM-EDS scanning, the GZ particles were prone to fracture under the TEM beam. Therefore, STEM-EDS line scanning was used for detection. In HAADF imaging, the central region of the GZ particles appeared dark. Line scanning of this central region revealed that the EDS data showed the presence of C, O, Mg, and Ca, with a negligible amount of Mg. The main elements were C, O, and Ca. Consequently, the low-contrast region in the centre of the GZ particles was likely caused by the difference in the crystalline structure between the central part and the surrounding areas of the particles.

We chose the particles in different morphologies, such as the spheres (NX, GC, and QH), cubes (DS), and tetragonal bipyramids (GZ), for XRD analysis (Fig. 4(d)). The result showed that the crystal structures of the five particles were the same although they displayed different form processes, which further confirmed that the particles were formed through assembly processes occurring above the crystalline structure level.

In summary, the formation of the aforementioned particles generally started with the aggregation of tiny crystals. These formed fusiform or other structural units underwent further multilayer aggregation to form spheres, cubes, and tetragonal bipyramids and then formed larger and well-ordered structures. These processes represented multistep and multilevel self-assembly behaviours.

4 Conclusions

After undergoing the freeze–thaw process, natural herbal decoctions could form well-defined and super-self-assembled particles. These particles exhibited unique morphologies that were specific to each herbal decoction. When different herbs were combined to create a decoction, the morphology of the particles from the freeze–thaw process changed accordingly. These results indicated that the complex mixture of the substances in the herbal decoctions influenced the morphology of the particles. Moreover, the super-self-assembled particles obtained from the combined herbal decoction continued to build upon the existing known particle structures, forming larger-scale super-self-assemblies.

In this study, the particle frameworks exemplified were primarily composed of calcium oxalate hydrates. These particles assemble into various morphologies (Fig. S4 in ESM) under the influence of different decoction components from the herbal formulas, even at the same crystalline structure (Fig. 4(d)). And from the experiment involving the addition of doxorubicin hydrochloride (Fig. S7 in ESM), and the TG-DTG analysis (Figs. 3(o) and 3(p)), we could infer that the organic components present in the decoction were mechanically incorporated between particles during the formation of these particles, resulting in the formation of organic–inorganic hybrid super-self-assemblies. Generally, these molecules of organic

components combined with the particles were relatively hydrophobic. Due to the highly complex composition of a herbal decoction, it was challenging to detail the molecular interactions between the organic and inorganic components and the mechanism behind the formation of different super-self-assemblies morphologies. However, the composition of a single herbal decoction was relatively stable, leading to well-structured and unique particle morphologies.

The specific assembly process of these super-self-assemblies could be observed using TEM. The particles were primarily composed of calcium oxalate hydrates and generally formed as spheres, cubes, and tetragonal bipyramids. Although their assembly behaviours differed during the formation process, they all interacted with the external solution environment.

These following trends suggested that the gel network structure serve as a precursor to the formation of super-assembled structures. During the freezing process of the decoction, the polysaccharides in herbal decoctions arrange themselves in an orderly manner, forming layered structures that signify the creation of the gel (Fig. S3 in the ESM, 0 min). As the decoction melted at room temperature, some of the gel network structures dissolved (such as those from the NX decoction), while others, with better thermal stability, remain intact, such as those from BS, HQ, and GG, and continue to form the final products alongside the super-self-assembled particles (as shown by ZZ in Fig. 2(b) and JG in Fig. S1 in the ESM). If this gel was extracted and heated, the gel network structure would break down and dissolve, leaving the particles as the final product. This indicated that the particles were encapsulated within the gel structure during their formation. The gel network always formed before the particles, and the formation of the particles was associated with these gel network structures. The morphology of super-self-assembled particles obtained by ion addition differed from those obtained through freeze–thawing because of the difference in the sol-gel state of the decoction.

According to our research, the structures of these super-self-assemblies are complex and varied. However, the preparation method is simple and environmentally friendly. These compounds can be obtained using the freeze–thaw process, and the addition of ions derived from the herbal decoctions can overcome the limitations of self-assemblies; these limitation include the relatively short lifetimes and the complex preparation processes. Our study provides significant contributions to the development of materials science. Due to the differing substance contents in herbal materials from various sources, the resulting super-self-assemblies vary, and these self-assemblies can be used for herbal identification in the future. In traditional Chinese medicine, practices involve using herbal formulations combined with mineral medicines. During this combination, these super-self-assemblies are formed, although they have not been explicitly reported before. In our previous work, we demonstrated that nanoparticles could interact with the body and be directionally transported through interstitial channels within the body [22, 23]. The findings from this study indicate that super-self-assemblies play a crucial role in soft matter medicine and have great potential in the biomedical field.

Herbal decoctions also produced intriguing fibrous structures through the freeze–thaw process (Fig. S9 in the ESM). Occasionally, disk-like morphologies could also be observed (Fig. S10 in the ESM). They came from different extraction site of JG&HQ decoction after freeze–thaw process. Moreover, these super-self-assemblies were not limited to herbal materials, and certain decoctions made from animal tissues also yielded unique assembled products after the freeze–thaw process. For example, the super-self-assembled particles generated from *Cicadae Periostracum* (CT) decoctions exhibited distinct morphologies (Fig. S11 in the ESM). Based on these results, super-self-assemblies are widely present in nature and warrant further development for potential applications in the future.

Electronic Supplementary Material: Supplementary material (the connections between iron ions and the decoction, changes in particle morphology, particle stability, drug-loading performance, biological effects, the preparation of assemblies with special structures, Table S1 and Figs. S1–S11) is available in the online version of this article at https://doi.org/10.26599/NR.2025.94907094.

Data availability

All data needed to support the conclusions in the paper are presented in the manuscript and the Electronic Supplementary Material. Additional data related to this paper may be requested from the corresponding author upon request.

Acknowledgements

We are grateful for support from Chinese Academy of Sciences for funding XDB3600000 (Nos. QYKIZD-SSW-SLH02 and ZDBS-LY-SLH036) and the Strategic Priority Research Program of the Chinese Academy of Sciences (No. XDB36000000).

Declaration of competing interest

All the contributing authors report no conflict of interests in this work.

Author contribution statement

D. H. and Z. A.: Research design. J. W. X. and Y. M.: Performing super-self-assemblies synthesis. J. W. X., Y. M., Q. Z., and N. W. Conducting activity tests. J. W. X., Y. M., M. Y. Z., and Z. X. L.: Data analysis. J. W. X., D. H., and Z. A.: Writing manuscript. All authors have read and approved the final submitted manuscript.

Use of AI statement

None.

References

[1] Li, X. L.; Zhang, W. J.; Lu, J. W.; Huang, L. X.; Nan, D. F.; Webb, M. A.; Hillion, F.; Wang, L. J. Templated biomineralization on self-assembled protein nanofibers buried in calcium oxalate raphides of *Musa* spp. *Chem. Mater.* **2014**, *26*, 3862–3869.

[2] Davila-Hernandez, F. A.; Jin, B.; Pyles, H.; Zhang, S.; Wang, Z. M.; Huddy, T. F.; Bera, A. K.; Kang, A.; Chen, C. L.; De Yoreo, J. J. et al. Directing polymorph specific calcium carbonate formation with de novo protein templates. *Nat. Commun.* **2023**, *14*, 8191.

[3] Fan, Q. H.; Zheng, Y.; Wang, X. C.; Xie, R. P.; Ding, Y.; Wang, B. Y.; Yu, X. Y.; Lu, Y.; Liu, L. Y.; Li, Y. L. et al. Dynamically re-organized collagen fiber bundles transmit mechanical signals and induce strongly correlated cell migration and self-organization. *Angew. Chem., Int. Ed.* **2021**, *60*, 11858–11867.

[4] Otter, L. M.; Eder, K.; Kilburn, M. R.; Yang, L.; O'Reilly, P.; Nowak,

D. B.; Cairney, J. M.; Jacob, D. E. Growth dynamics and amorphous-to-crystalline phase transformation in natural nacre. *Nat. Commun.* **2023**, *14*, 2254.

[5] Gordon, L. M.; Joester, D. Nanoscale chemical tomography of buried organic–inorganic interfaces in the chiton tooth. *Nature* **2011**, *469*, 194–197.

[6] Song, Q. T.; Li, Y.; Jin, Z. C.; Liu, H.; Creyer, M. N.; Yim, W.; Huang, Y. P.; Hu, X. B.; He, T. Y.; Li, Y. J. et al. Self-assembled homopolymeric spherulites from small molecules in solution. *J. Am. Chem. Soc.* **2023**, *145*, 25664–25672.

[7] Cho, N. H.; Guerrero-Martínez , A.; Ma, J.; Bals, S.; Kotov, N. A.; Liz-Marzán , L. M.; Nam, K. T. Bioinspired chiral inorganic nanomaterials. *Nat. Rev. Bioeng.* **2023**, *1*, 88–106.

[8] Jiang, W. F.; Qu, Z. B.; Kumar, P.; Vecchio, D.; Wang, Y. F.; Ma, Y.; Bahng, J. H.; Bernardino, K.; Gomes, W. R.; Colombari, F. M. et al. Emergence of complexity in hierarchically organized chiral particles. *Science* **2020**, *368*, 642–648.

[9] Fu, H. L.; Huang, J. Y.; van der Tol, J. J. B.; Su, L.; Wang, Y. Y.; Dey, S.; Zijlstra, P.; Fytas, G.; Vantomme, G.; Dankers, P. Y. W. et al. Supramolecular polymers form tactoids through liquid–liquid phase separation. *Nature* **2024**, *626*, 1011–1018.

[10] Li, T.; Wang, P. L.; Guo, W. B.; Huang, X. M.; Tian, X. H.; Wu, G. R.; Xu, B.; Li, F. F.; Yan, C.; Liang, X. J. et al. Natural berberine-based Chinese herb medicine assembled nanostructures with modified antibacterial application. *ACS Nano* **2019**, *13*, 6770–6781.

[11] Yao, L.; Zhao, M. M.; Luo, Q. W.; Zhang, Y. C.; Liu, T. T.; Yang, Z.; Liao, M.; Tu, P. F.; Zeng, K. W. Carbon quantum dots-based nanozyme from coffee induces cancer cell ferroptosis to activate antitumor immunity. *ACS Nano* **2022**, *16*, 9228–9239.

[12] Li, X. Y.; Liang, Z.; Du, J. C.; Wang, Z. Q.; Mei, S.; Li, Z. Q.; Zhao, Y.; Zhao, D. D.; Ma, Y. M.; Ye, J. et al. Herbal decoctosome is a novel form of medicine. *Sci. China Life Sci.* **2019**, *62*, 333–348.

[13] Fan, J. M.; Yu, H.; Lu, X.; Xue, R.; Guan, J. W.; Xu, Y.; Qi, Y. Y.; He, L. Y.; Yu, W.; Abay, S. et al. Overlooked spherical nanoparticles exist in plant extracts: From mechanism to therapeutic applications. *ACS Appl. Mater. Interfaces* **2023**, *15*, 8854–8871.

[14] Meldrum, F. C.; Cölfen, H. Controlling mineral morphologies and structures in biological and synthetic systems. *Chem. Rev.* **2008**, *108*, 4332–4432.

[15] Guo, X. H.; Luo, W. K.; Wu, L. Y.; Zhang, L. L.; Chen, Y. X.; Li, T.; Li, H. G.; Zhang, W.; Liu, Y. W.; Zheng, J. et al. Natural products from herbal medicine self-assemble into advanced bioactive materials. *Adv. Sci. (Weinh.)* **2024**, *11*, e2403388.

[16] Tang, L. J.; Di, Z. H.; Zhang, J. F.; Yin, F. Y.; Li, L. L.; Zheng, L. Coordination-driven self-assembly of metallo-nanodrugs for local inflammation alleviation. *Nano Res.* **2023**, *16*, 13259–13266.

[17] Liang, R. J.; Li, R.; Mo, W. D.; Zhang, X. Z.; Ye, J. C.; Xie, C.; Li, W. Y.; Peng, Z.; Gu, Y. Q.; Huang, Y. X. et al. Engineering biomimetic silk fibroin hydrogel scaffolds with “organic–inorganic assembly” strategy for rapid bone regeneration. *Bioact. Mater.* **2024**, *40*, 541–556.

[18] Liu, C.; Du, W. C.; Zhang, L.; Wang, J. C. Natural synergy: Oleanolic acid-curcumin co-assembled nanoparticles combat osteoarthritis. *Colloid Surf. B* **2025**, *245*, 114286.

[19] Johnson, G.; Yang, M. Y.; Liu, C.; Zhou, H.; Zuo, X. B.; Dickie, D. A.; Wang, S. H.; Gao, W. P.; Anaclet, B.; Perras, F. A. et al. Nanocluster superstructures assembled via surface ligand switching at high temperature. *Nat. Synth.* **2023**, *2*, 828–837.

[20] Lv, J. W.; Gao, X. Q.; Han, B.; Zhu, Y. F.; Hou, K.; Tang, Z. Y. Self-assembled inorganic chiral superstructures. *Nat. Rev. Chem.* **2022**, *6*, 125–145.

[21] Tan, C. X.; Wang, Y. L. Self-assembly of *Ophiopogonis* polysaccharide-iron(III) complex in aqueous solution and solid state. *J. Chin. Pharm. Sci.* **2019**, *28*, 665–672.

[22] Sun, Q. M.; Shi, X. L.; Feng, J. T.; Zhang, Q.; Ao, Z.; Ji, Y. L.; Wu, X. C.; Liu, D. S.; Han, D. Cytotoxicity and cellular responses of gold nanorods to smooth muscle cells dependent on surface chemistry coupled action. *Small* **2018**, *14*, 1803715.

[23] Hu, N.; Shi, X. L.; Zhang, Q.; Liu, W. T.; Zhu, Y. T.; Wang, Y. Q.; Hou, Y.; Ji, Y. L.; Cao, Y. P.; Zeng, Q. et al. Special interstitial route can transport nanoparticles to the brain bypassing the blood–brain barrier. *Nano Res.* **2019**, *12*, 2760–2765.